

Inverse Liner Z-Pinch: An Experimental Pulsed Power Platform for Studying Radiative Shocks

T. Clayson[✉], S. V. Lebedev, F. Suzuki-Vidal, G. C. Burdiak, J. W. D. Halliday,
J. D. Hare, J. Ma, L. G. Suttle, E. R. Tubman

Abstract—We present a new experimental platform for studying radiative shocks using an “inverse liner z-pinch” configuration. This platform was tested on the MAGPIE pulsed power facility (~ 1 MA with a rise time of ~ 240 ns) at Imperial College London, U.K. Current is discharged through a thin-walled metal tube (a liner) embedded in a low-density gas-fill and returned through a central post. The resulting magnetic pressure inside the liner launched a cylindrically symmetric, expanding radiative shock into the gas-fill at ~ 10 km/s. This experimental platform provides good diagnostic access, allowing multiframe optical self-emission imaging, laser interferometry, and optical emission spectrography to be fielded. Results from experiments with an Argon gas-fill initially at 0.04 mg/cm³ are presented, demonstrating the successful production of cylindrically symmetric, expanding shocks that exhibit radiative effects such as the formation of a radiative precursor.

Index Terms—Pulsed power, radiative shocks.

I. INTRODUCTION

RADIATIVE effects occur in high mach number shocks when the radiative flux from the thermal emission of the hot postshock material is nonnegligible, resulting in significant changes to the shock structure and the formation of a radiative shock [1], [2]. Understanding these phenomena is of great importance to the high energy density physics community due to their presence in inertial confinement fusion implosions [3] and their abundance in astrophysical events [4].

Radiation emitted by the postshock material results in radiative cooling and thus an increase in postshock compression (exceeding the maximum compression in a nonradiating shock of $4\times$ for an adiabatic index of $5/3$) [1], [2], [5]. In some cases, this could lead to the onset of instabilities such as the Vishniac thin-shell overstability [6]–[8]. In addition, material ahead of the shock front is able to reabsorb this radiation,

resulting in photoionization and heating of the preshock material. This manifests itself as a radiative precursor, a layer of heated and ionized gas ahead of the shock front [2].

It is possible to produce radiative shocks in laboratory experiments using lasers focused onto a pin embedded in a gas [9], a cluster gas [10]–[12], or a piston attached to a gas cell [13]–[21]. Radiative shocks have also been produced on pulsed power generators using imploding liners with an internal gas fill [22]–[24]. In these experiments, ~ 1 MA of current was discharged through a gas-filled liner (a thin-walled metal tube). The liner did not move on the time scales of the experiment and, instead, multiple cylindrically converging radiative shocks were observed launched into a low-density gas that filled the liner. These shocks exhibited radiative effects such as the formation of a radiative precursor. However, the limited radius of the liners (3 mm) prevented the shocks evolving unimpeded, with the radiative precursor extending over a similar length scale.

This paper introduces a new experimental platform for studying radiative shocks that were demonstrated on the MAGPIE pulsed power facility (~ 1 MA with a rise time of ~ 240 ns) [25] at Imperial College London, U.K. This platform uses an “inverse liner z-pinch” setup to produce cylindrically expanding radiative shocks that are able to propagate unimpeded for several microseconds over a distance of 50 mm. The experimental results presented here show that the radiative shocks are reproducible and initially uniform, allowing this platform to be used for benchmarking numerical radiative-hydrodynamic simulations and studying radiative instabilities.

II. EXPERIMENTAL SETUP

The experimental platform for the inverse liner z-pinch setup is shown in Fig. 1. A 3-D diagram depicting how the shocks are driven is shown in Fig. 1(a). The ~ 1 -MA current of the MAGPIE generator [25] was discharged through a 20-mm-long stainless steel liner with an inner diameter of 11 mm and a wall thickness of $100\ \mu\text{m}$. The current was then returned through a 5-mm-diameter cylindrical electrode on the axis, generating a toroidal magnetic field with a peak of ~ 40 T on the inner surface of the liner. The resulting magnetic pressure of ~ 400 MPa resulted in a cylindrically symmetric, radially expanding shock, propagating at ~ 10 km/s, being launched into an Argon gas-fill initially at 0.04 mg/cm³. The liner did not move on the time scale of the experiment and did not melt. A 3-D cutaway of a CAD model is shown in Fig. 1(b), with

Manuscript received January 2, 2018; revised June 4, 2018; accepted June 9, 2018. Date of publication October 5, 2018; date of current version November 8, 2018. This work was supported in part by the Engineering and Physical Sciences Research Council through a DTA Studentship and in part by the U.S. Department of Energy under Award DE-F03-02NA00057 and Award DE-SC-0001063. The review of this paper was arranged by Senior Editor F. Beg. (Corresponding author: T. Clayson.)

T. Clayson and G. C. Burdiak were with the Blackett Laboratory, Imperial College, London SW7 2AZ, U.K. They are now with First Light Fusion Ltd, Oxford OX5 1QU, U.K. (e-mail: thomasalbertclayson@gmail.com).

S. V. Lebedev, F. Suzuki-Vidal, J. W. D. Halliday, J. D. Hare, L. G. Suttle, and E. R. Tubman are with the Blackett Laboratory, Imperial College, London SW7 2AZ, U.K.

J. Ma is with the Northwest Institute of Nuclear Technology, Xian 710024, China.

Color versions of one or more of the figures in this paper are available online at <http://ieeexplore.ieee.org>.

Digital Object Identifier 10.1109/TPS.2018.2868757

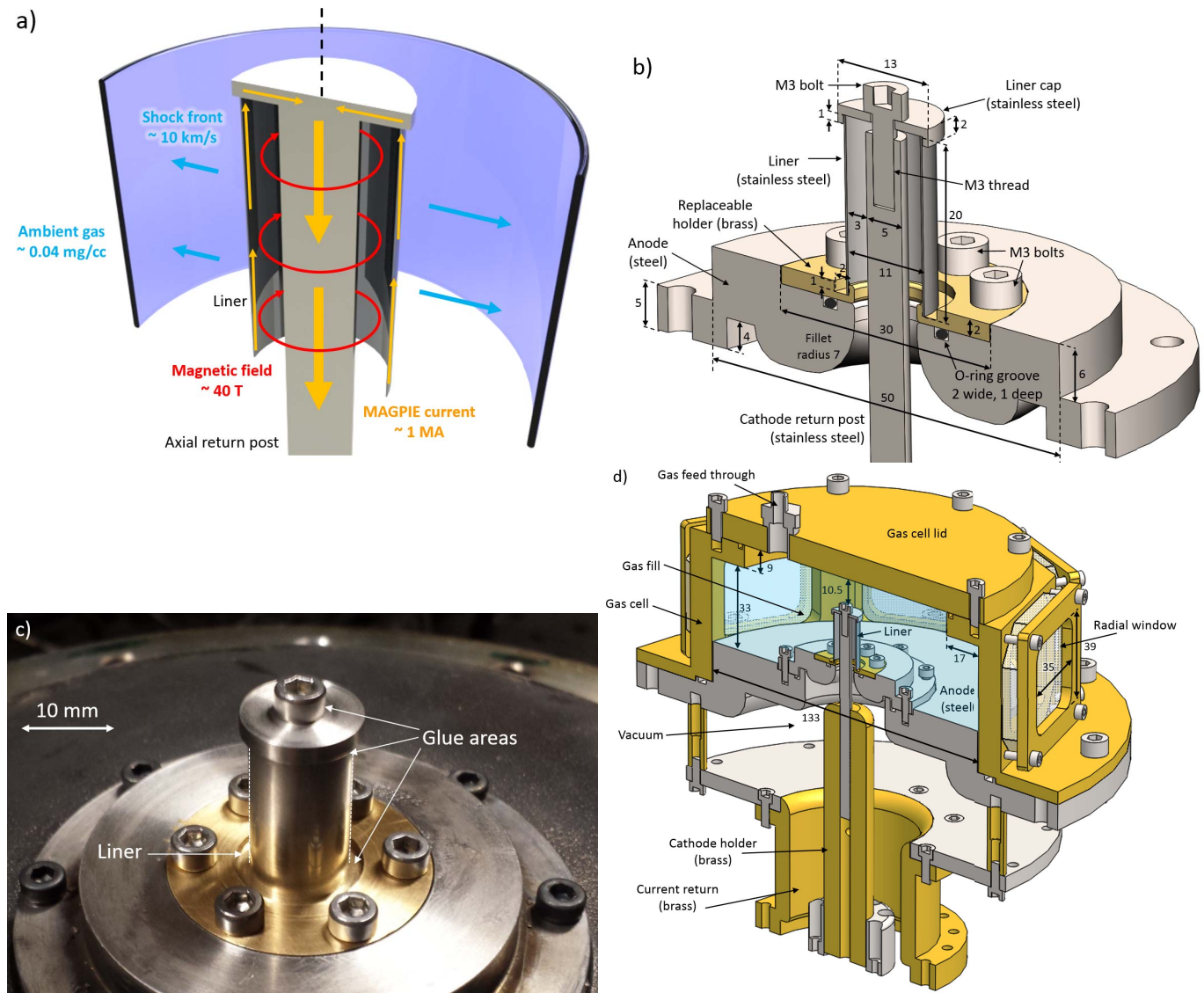


Fig. 1. (a) 3-D diagram of the “inverse liner” experimental setup highlighting the current path in yellow, toroidal magnetic field in red, and radially expanding shock in blue. (b) 3-D cutaway of a CAD model, dimensions in millimeters. (c) Photograph of the liner in the MAGPIE experimental chamber. (d) 3-D cutaway of a CAD model of the experimental hardware and gas cell, dimensions in millimeters.

all dimensions in millimeters, and a photograph of the liner in the MAGPIE chamber is shown in Fig. 1(c).

The MAGPIE transfer line delivering current to the liner is kept under vacuum and so a uniform gas-fill around the liner was provided by a separate gas-cell, shown in the 3-D cutaway in Fig. 1(d). This gas cell provided a large volume with an internal radius of 66.5 mm and height of 33 mm, allowing shocks to evolve unimpeded for several microseconds. The gas cell exterior was octagonally shaped allowing for eight radially facing windows, each with a height of 35 mm and a width of 39 mm, providing a side on diagnostic access to the experiment.

The short distance between the liner and the axial electrode (3 mm) required the interior of the liner to be under vacuum to prevent electrical breakdown, and so the liner formed part of the gas seal. To create a gas-tight seal between the liner and the rest of the hardware, clamps and rubber O-rings were used. However, these reduced the effective liner length to ~11 mm

and also drove large edge effects. Later experiments instead used a coating of Araldite Instant [26] (a two-component epoxy adhesive that begins setting in 90 s) around the joints between the liner and hardware, which reduced the magnitude of these edge effects and increased the effective liner length.

The diagnostic setup is depicted in Fig. 2. All diagnostics were imaged along the same line of sight, allowing for direct comparisons. A Mach-Zehnder laser interferometer was fielded to measure the electron density both ahead and behind the shock. The second harmonic of an stimulated Brillouin scattering compressed, pulsed Nd-YAG laser (EKSPLA SL321P) was used to produce a ~0.5-ps pulse with a wavelength of 532 nm, which was then recorded with a commercial Canon DSLR with an exposure greater than the experiment duration. Optical self-emission from the plasma was recorded with a high-speed, multiframe camera (Invisible Vision U2V1224) on 12 images with exposures of 10 ns and an interframe time of 40 ns. A low pass

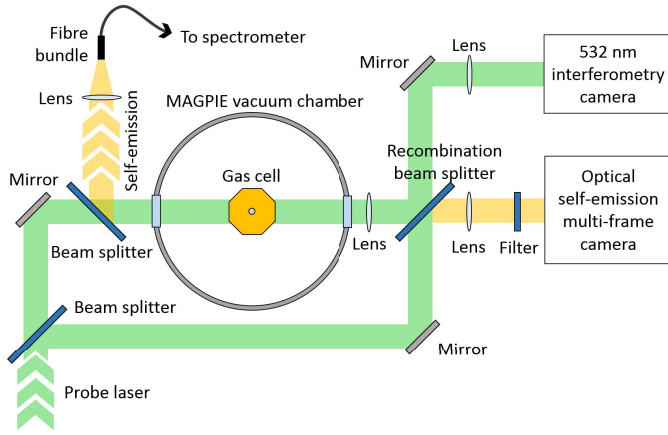


Fig. 2. Diagnostic setup is shown in the top down diagram. Laser interferometry, self-emission multiframe, and optical spectroscopy were all performed along the same line of sight.

filter was inserted in front of this camera to block the laser light and so this diagnostic was sensitive to wavelengths >600 nm. In addition, a bundle of 14 optical fibers imaged the plasma self-emission from ~ 250 - μm -diameter collection volumes spaced 580 μm apart, radially away from the liner surface. These were imaged onto an ANDOR SR-500i-A spectrometer with a 400-lines/mm grating and exposure of 8 ns, recording spectra between 435 and 490 nm.

III. EXPERIMENTAL RESULTS

A time sequence of current through the liner and timings of diagnostics are shown for two similar experiments, with the same Argon gas-fill initially at 0.04 mg/cm^3 , in Fig. 3. The current was determined with two Rogowski coils and the increased current was found to result in slightly increased shock velocities, with ~ 13 km/s measured for Fig. 3(a) with a peak current of ~ 1.2 MA and 10 km/s measured for Fig. 3(b) with a peak current of ~ 1.1 MA.

A. Optical Self-Emission

The evolution of the radiative shocks was studied with the multiframe camera that recorded 12 images from a single experiment. A selection of images from a typical experiment [Fig. 3(a)] is shown in Fig. 4(a). The liner can be seen as the dark region in the center, labeled in the top image. Although 20 mm long in total, this experiment used the initial design with O-ring clamps which reduced the effective liner length to ~ 11 mm. The shock can be seen as bright emission to the left and right of the liner, labeled in the second image, propagating radially outwards from the liner surface.

Additional shocks were launched from the top and bottom of the liner due to the interaction with the surrounding hardware, labeled as “edge shocks” in the bottom image. All measurements were, therefore, made along the midheight of the liner where the primary radial shock remained uniform.

To measure the shock velocity, a horizontal lineout was taken at a height of 5 mm [shown in the third image of Fig. 4(a)] averaged vertically over 200 μm . In each lineout, the shock front position was then identified as the rising edge in the intensity profile. Measurements from both the left and

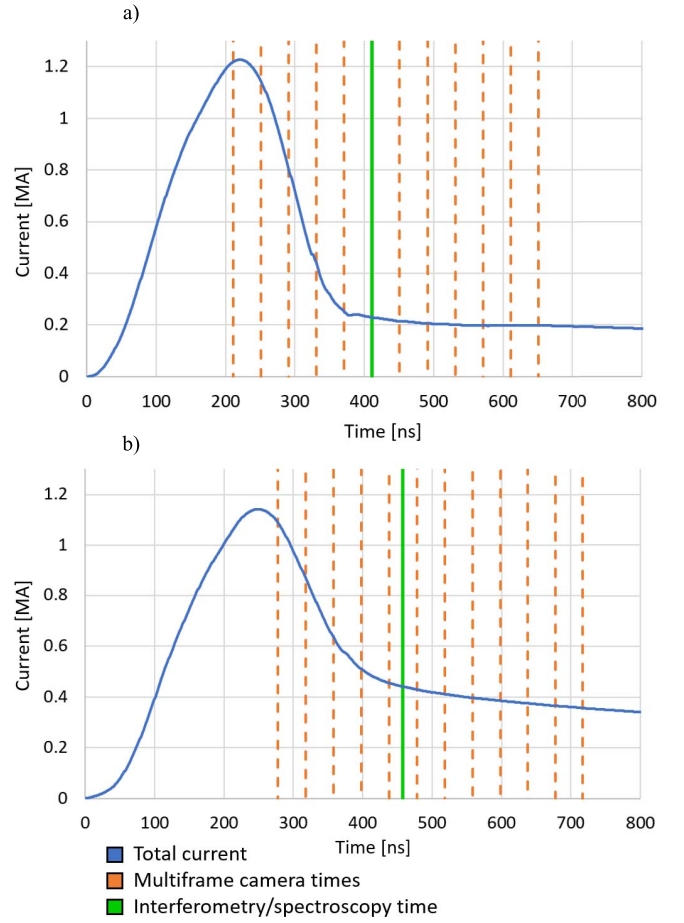


Fig. 3. Current through the liner as a function of time for two identical experiments. Timings of different diagnostics are indicated. (a) s0623_16. (b) s1212_16.

right sides of Fig. 4(a) are plotted as a function of time after current start in Fig. 4(b). Error bars have been set to the minimum resolution of the multiframe camera at which features may be resolved, measured to be ~ 630 μm (motion blurring due to the velocity of the shock is expected to be in the order of 100 μm). Positions from both the left and right shocks follow a near identical trajectory indicating that the current was discharged uniformly through the liner resulting in cylindrically symmetric expanding shocks. These points closely follow a linear trendline indicating that the shock velocity remains constant over the observed time, ~ 500 ns.

Measurements from 14 separate experiments indicate shocks propagated at a constant velocity between 7 and 13 km/s, depending on the MAGPIE drive current. In addition, the shock launch time was determined by extrapolating trendlines to the liner surface at 5.6 mm. This yielded a launch time of 187 ± 24 ns after the current start. These launch times are comparable to those seen in previous converging shock experiments [24] while velocities are slower by a factor of 2 (~ 10 km/s instead of ~ 20 km/s) primarily due to the increased mass density of the gas-fill. However, in contrast to the multiple shocks observed in converging shock experiments, only a single shock (ignoring edge effects) is observed in the experiments described in this paper. The larger liner diameter

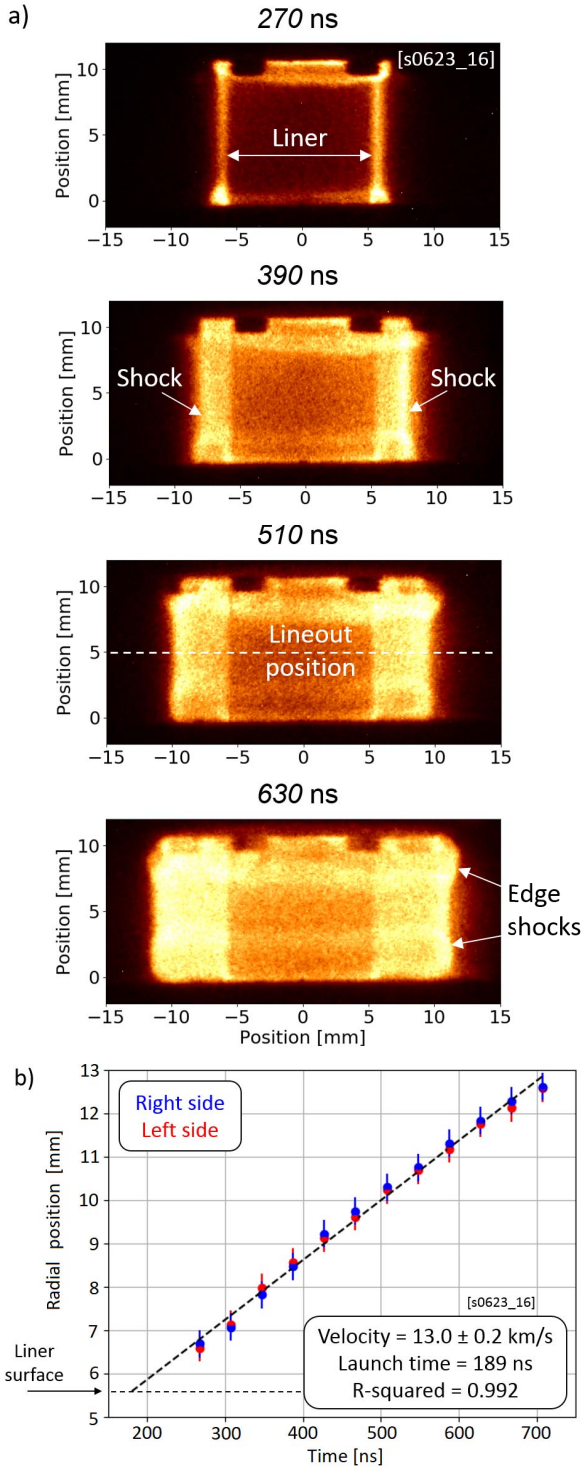


Fig. 4. (a) Optical self-emission images from the shot shown in Fig. 3(a). The liner is seen as the dark region in the center while the shocks expand radially and can be seen as regions of bright emission. (b) Shock front position plotted as a function of time. A linear trend line, shown with a dashed line closely fits the data allowing the velocity to be determined.

(11 mm instead of 6 mm) resulted in less ohmic heating that was insufficient to melt the liner.

B. Laser Interferometry

Laser interferometry records variations in refractive index of the plasma as fringe shifts in an interferogram. An example

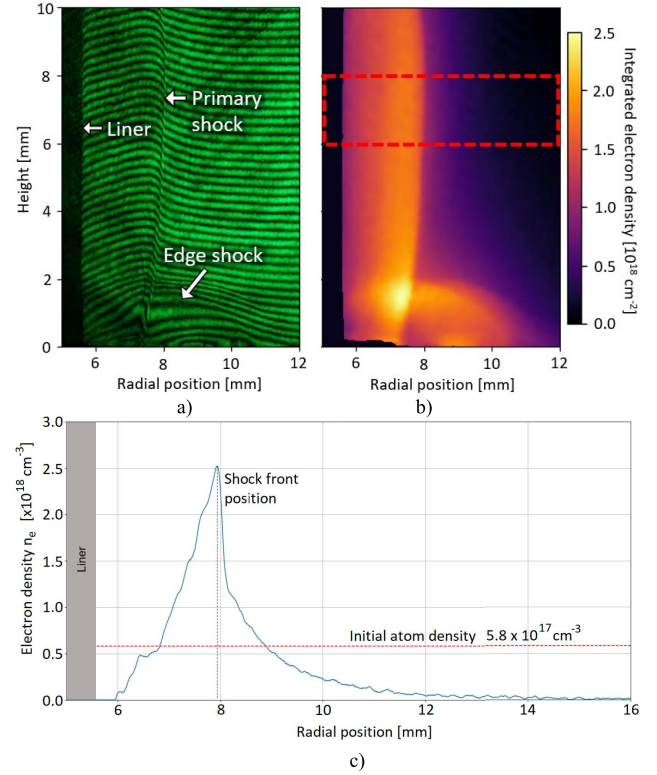


Fig. 5. (a) Interferometry image from the experiment shown in Fig. 3(b) taken at 460 ns. (b) Processed image showing a map of electron density integrated along the probe beams path, $n_e L$. (c) Lineout taken from the hashed position marked in (b) has been Abel inverted showing electron density as a function of radius.

image [from the experiment shown in Fig. 3(b)] is shown in Fig. 5(a), taken 460 ns after current start. To maximize the spatial resolution, the laser interferometry used a higher magnification, imaging a 12×10 mm field of view on one side of the liner. Due to the cylindrical symmetry of the system, this was representative of the entire radially expanding shock. The surface of the liner is visible to the left (< 5.6 mm) and the shock propagates to the right, with the shock front visible as a steep shift in fringes at ~ 8 mm.

The shift of these fringes is proportional to the electron density integrated along the path of the beam, $n_e L$, and thus these images can be used to produce 2-D maps of $n_e L$ following the procedure described in [27]. The resulting map is shown in Fig. 5(b).

Edge effects are more prominent in these images and a large “edge shock” can be seen at the base of the liner which interacts with the primary shock, resulting in regions of enhanced electron density. In addition, the primary shock bends toward the edge of the liner, slightly deviating from the approximately 1-D cylindrical expansion.

A horizontal lineout of $n_e L$ was taken through the region that highly resembled a 1-D expansion, averaged between a height of 6 and 8 mm [indicated by the hashed area in Fig. 5(b)]. This $n_e L$ profile was used to determine the electron density as a function of radius using an Abel inversion. The result is shown in Fig. 5(c) together with the initial atom density of $n_i = 5.8 \times 10^{17} \text{ cm}^{-3}$ indicated with a dashed red line.

A peak electron density of $2.5 \times 10^{18} \text{ cm}^{-3}$ at a radial position of 7.95 mm corresponds with the shock front position. Dividing by the initial gas-fill atom density yields a peak ionization of $Z \sim 4$ for the radiative precursor. Behind the shock front, the electron density rapidly decreases suggesting that the shock is similar to a blast wave with an expanding thin shell of dense material followed by hot, low-density gas.

Without radiative effects, ionization ahead of the shock front would be expected to be zero. Instead, the interferometry shows that the electron density decays gradually over ~ 4 mm ahead of the shock front, indicating that the unshocked material is being ionized and thus a precursor is formed. This is similar to results from converging shock experiments [22]–[24].

C. Optical Spectroscopy

To obtain an independent estimate of the level of ionization in both the precursor and shocked materials, the optical spectroscopy was fielded on the experiment shown in Fig. 3(a). Self-emission spectra between 435 and 490 nm were recorded from 14 points spaced radially outwards from the liner surface, 3 of which are shown in Fig. 6(a). Spectra from the postshock region (fiber 1), the approximate shock front position (fiber 5), and the precursor (fiber 9) are shown in Fig. 6(b). For the clarity of presentation, the spectrum from the precursor region has been multiplied by a factor of 5.

The spectra bear remarkable similarities and the same lines are present in all spectra. However, the spectra from the precursor region are significantly dimmer than that from the shock front. Persistent lines of Ar-II are present in these spectra, such as the $3s^2 3p^4 4p$ to $3s^2 3p^4 4s$ transitions at 461.0 and 480.6 nm. However, the lack of significant Ar-III contribution, such as the $3s^2 3p^3 4p$ to $3s^2 3p^3 3d$ transitions at 456.5 and 468.8 nm suggest that the plasma is only singly ionized in both the postshock and precursor regions.

To improve on this estimate, the atomic physics code PrismSPECT [28] was used to simulate the expected spectrum at various points in the radiative precursor. Simulations were run for an Argon plasma at 0.04 mg/cm^3 , at a variety of temperatures, with detailed configuration accounting, the low-temperature spectroscopy atomic model and zero width. As an initial estimate, the plasma was assumed to be in steady state, which may not be accurate for the precursor region. By visually comparing the presence of lines in the calculated spectrum with that obtained in experiments, the temperature was estimated to be 1.5–2.5 eV [the simulated spectrum for a plasma at 2.5 eV is shown in Fig. 6(c)] with an average ionization of $Z = 0.5$ –1.2 at all points in the radiative precursor and postshock region, similar to results from converging shock experiments [23].

IV. DISCUSSION

A. Temperature Across the Shock

The postshock ion temperature, T_i may be estimated to be [2], [5]

$$T_i = 2 \frac{\gamma - 1}{k_B(\gamma + 1)^2} \frac{Am_p}{Z + 1} u_s^2 \quad (1)$$

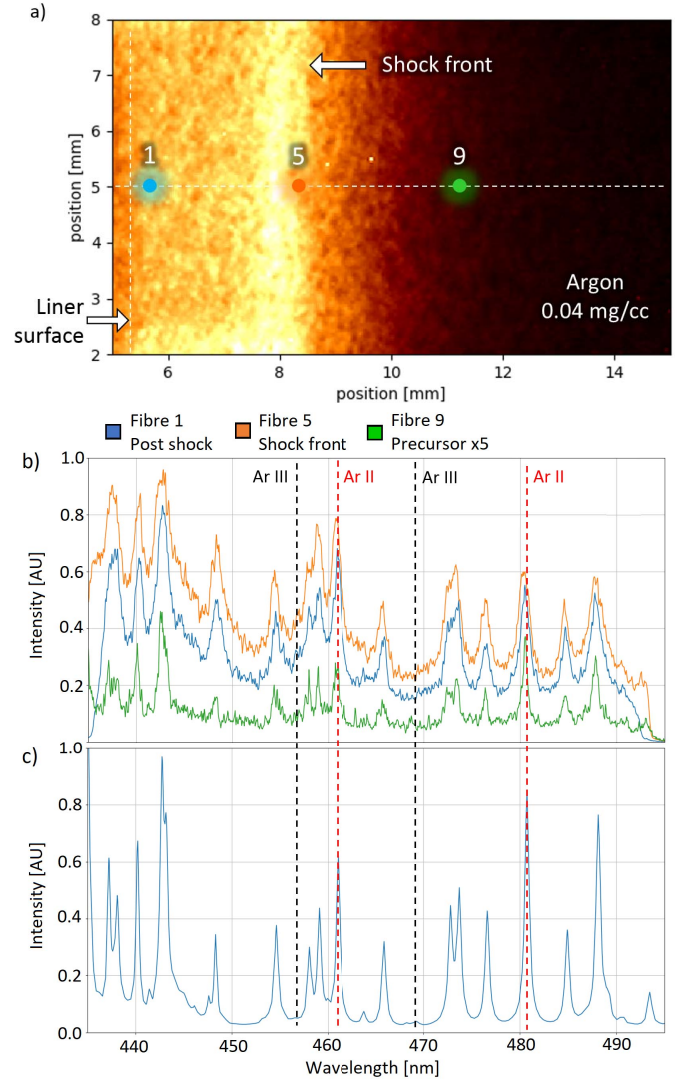


Fig. 6. (a) Focal points of several fibers superimposed on a self-emission image taken at approximately the same time. (b) Spectrum recorded from the experiment shown in Fig. 3(a) taken at 410 ns. (c) PrismSPECT simulated spectrum for an Argon plasma at 0.04 mg/cm^3 and 2.5 eV.

where γ is the adiabatic index (assumed to be $\gamma = 5/3$ for a monatomic gas such as Argon), k_B is Boltzmann's constant, A is the relative atomic mass (39.9 for Argon), m_p is the proton mass, Z is the average ionization, and u_s is the shock velocity (found to be $\sim 10^4$ m/s). Assuming that the postshock ionization is not dissimilar to the peak ionization observed in the precursor (found to be $Z \sim 4$ in Fig. 7) yields a temperature of 1.6 eV, agreeing with optical spectroscopy estimates of 1.5–2.5 eV.

B. Formation of the Radiative Precursor

The precursor observed in these experiments is expected to have formed due to the reabsorption of radiation emitted by the shock front. However, precursors ahead of the shock may also form due to particles reflected by the shock front depositing their energy ahead of the shock or due to the thermal conduction [2].

To determine if electron or ion acceleration plays a role, the electron and ion mean free paths were calculated

using [29]

$$\lambda_e(\text{cm}) = 2 \times 10^{18} \frac{[T_e(\text{KeV})]^2}{Z n_e(\text{cm}^{-3})} \quad (2)$$

$$\lambda_i(\text{cm}) = 2 \times 10^{18} \frac{[T_i(\text{KeV})]^2}{Z^3 n_e(\text{cm}^{-3})} \quad (3)$$

where T_e and T_i are the electron and ion temperatures, respectively, and n_e is the electron density. Temperature and ionization estimates were taken from the optical spectroscopy, assuming $T_i = T_e \sim 2$ eV and $Z \sim 0.9$. The electron density was calculated by multiplying the gas-fill initial atom density by the ionization, yielding $n_e = 4.6 \times 10^{17} \text{ cm}^{-3}$. This yielded a mean free path of $\lambda_e \sim 190$ nm and $\lambda_i \sim 240$ nm for the electron and ions, respectively, both of which are significantly smaller than the observed precursor. However, to fully discount this mechanism, the mean free path was recalculated for ions traveling at the shock velocity with a kinetic energy of ~ 21 eV. This yielded a larger ion mean free path of $\sim 26 \mu\text{m}$ but still significantly smaller than the observed precursors scale and below the resolution of the laser interferometry diagnostic. Thus, this mechanism may be ignored in this system.

To determine if the thermal conduction was responsible for the formation of the precursor, the thermal diffusion was approximated as a Marshak wave [2] where the conductivity, k_{th} , is given as

$$k_{\text{th}} = 2 \times 10^{21} \frac{[T_e(\text{eV})]^{5/2}}{\ln(\Lambda) Z(Z+1) n_i(\text{cm}^{-3})} C_p \rho \quad (4)$$

where $\ln(\Lambda)$ is the Coulomb logarithm (assumed to be ~ 4 for these plasma conditions), C_p is the heat capacity at constant pressure ($\sim 5.2 \times 10^6$ erg/g/K for Argon [30]), and ρ is the density (in g/cm³) of the unshocked medium. Using the previous estimates for temperature and ionization, $T_e \sim 2$ eV and $Z \sim 0.9$, yields a conductivity of $k_{\text{th}} \sim 5.9 \times 10^5$ g.cm/s³K. The position of the thermal wavefront, x_0 , in a Marshak wave as a function of time, t , is given as [2]

$$x_0 = \frac{\sqrt{n+2}}{n+1} \sqrt{\frac{2k_{\text{th}}}{\rho C_V}} \sqrt{2t} \quad (5)$$

where n is a dimensionless number, ~ 4 in high density materials [2], and C_V is the heat capacity at constant volume. Using the electron thermal conductivity previously calculated and assuming the process is approximately adiabatic (so that $C_V = C_P/\gamma$) indicates that the Marshak wave has propagated ~ 0.3 mm after ~ 200 ns (the time between the shock being launched and the interferometry image). This is insufficient to account for the large precursor observed ahead of the shock front. However, this should be resolvable by the interferometry diagnostic and may partially contribute to the precursor directly ahead of the shock front. However, this model does not take into account the motion of the shock front itself and, thus, is likely to be a significant overestimate.

C. LTE in the Radiative Precursor

Estimates of ionization throughout the precursor from interferometry were found by dividing the electron density by the initial gas-fill atom density, yielding the plot shown in Fig. 6.

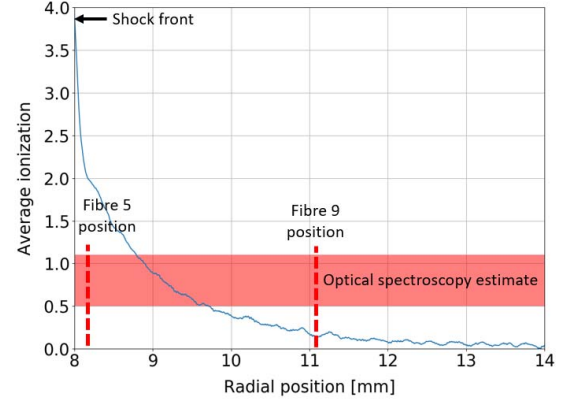


Fig. 7. Ionization in the precursor, determined by dividing the electron density shown in Fig. 5 by the gas fill initial atom density. The range of ionizations estimated from the optical spectroscopy is highlighted in red and shows poor agreement with estimates from interferometry.

This shows a gradually decreasing ionization, while the optical spectroscopy shows a similar spectrum at all regions in the precursor, suggesting a constant temperature and ionization. For example, the optical spectroscopy taken ~ 3 mm ahead of the shock front, shown in the green curve in Fig. 7(a), estimates an ionization of $Z = 0.5\text{--}1.2$, while the laser interferometry estimates an electron density of $\sim n_e = 1 \times 10^{17}$ corresponding with an average ionization of $Z \sim 0.2$. These observations match those in [23] in which it was suggested that the precursor is not in local thermal equilibrium (LTE) and photoionization results in a small fraction of ions dominating the emission spectrum. To verify this, the ion collision times were estimated for different regions in the precursor using [29]

$$\tau_i = 4 \times 10^{12} \frac{\sqrt{A} [T_i(\text{KeV})]^{2/3}}{Z^3 n_e(\text{cm}^{-3})}. \quad (6)$$

This yielded collision times of $\tau_i(r = 9 \text{ mm}) = 10$ ns, $\tau_i(r = 10 \text{ mm}) = 680$ ns, and $\tau_i(r = 11 \text{ mm}) = 11 \mu\text{s}$. A shock with a velocity of ~ 10 km/s propagates 1 mm in 100 ns. Therefore, the region at $r = 9$ mm (~ 1 mm ahead of the shock front) has sufficient time for many ion collisions and, thus, is expected to be approximate LTE state, while more distant regions have insufficient time to thermalize and thus are likely to be in non-LTE. This confirms conclusions suggested in [23].

V. CONCLUSION

A novel platform for studying radiative shocks has been demonstrated on the MAGPIE pulsed power facility (~ 1 MA in 240 ns) at Imperial College London, U.K. This platform is capable of producing cylindrically expanding radiative shocks that propagate at a constant velocity of ~ 10 km/s for over 500 ns in an Argon gas-fill initially at 0.04 mg/cm^3 . The formation of a radiative precursor is observed, extending ~ 3 mm ahead of the shock front. The interferometry and the optical spectroscopy were found to disagree on ionization in the radiative precursor region. This suggests that the radiative precursor is not in LTE and photoionization results in a small fraction of ionized ions dominating the emission spectrum. These experiments have been expanded to include a range of

other gas-fills, allowing these radiative shocks to be characterized for a range of elements, to be detailed in the future publications.

The uniformity and reproducibility of the radiative shocks produced with this platform make it suitable for the study of perturbed radiative shocks and radiative instabilities. Controllable perturbations may be seeded into the shock by carving grooves on the surface of the liner. The spacing and the depth of these grooves allow the wavelength and the amplitude of perturbations in the radiative shock to be controlled. This has been experimentally verified. By seeding perturbations of a specific wavelength, it is hoped that this setup could be used to study radiative plasma instabilities such as the Vishniac instability [6]. This will be the subject of future publications.

ACKNOWLEDGMENT

The authors would like to thank the Imperial College London Institute of Shock Physics for the use of their multiframe camera.

REFERENCES

- [1] Y. B. Zel'dovich and Y. P. Raizer, *Physics of Shock Waves and High-Temperature Hydrodynamic Phenomena*. New York, NY, USA: Dover, 2002.
- [2] R. P. Drake, *High-Energy-Density Physics: Foundation of Inertial Fusion and Experimental Astrophysics*. Berlin, Germany: Springer, 2006.
- [3] A. Pak *et al.*, "Radiative shocks produced from spherical cryogenic implosions at the national ignition facility," *Phys. Plasmas*, vol. 20, no. 5, p. 056315, 2013.
- [4] B. A. Remington, R. P. Drake, and D. D. Ryutov, "Experimental astrophysics with high power lasers and Z pinches," *Rev. Modern Phys.*, vol. 78, no. 3, p. 755, 2006.
- [5] R. P. Drake, "Radiative shocks in the laboratory," *Astrophys. Space Sci.*, vol. 298, pp. 49–59, 2005.
- [6] E. T. Vishniac, "The dynamic and gravitational instabilities of spherical shocks," *Astrophys. J.*, vol. 274, pp. 152–167, Nov. 1983.
- [7] J. M. Laming and J. Grun, "Dynamical overstability of radiative blast waves: The atomic physics of shock stability," *Phys. Rev. Lett.*, vol. 89, no. 12, p. 125002, 2002.
- [8] J. Grun, C. Manka, J. Resnick, R. Burris, J. Crawford, and B. H. Ripin, "Instability of Taylor–Sedov blast waves propagating through a uniform gas," *Phys. Rev. Lett.*, vol. 66, no. 22, p. 3200, 1991.
- [9] A. D. Edens *et al.*, "Study of high mach number laser driven blast waves in gases," *Phys. Plasmas*, vol. 17, no. 11, p. 112104, 2010.
- [10] M. J. Edwards *et al.*, "Investigation of ultrafast laser-driven radiative blast waves," *Phys. Rev. Lett.*, vol. 87, no. 8, p. 085004, 2001.
- [11] A. S. Moore *et al.*, "Full-trajectory diagnosis of laser-driven radiative blast waves in search of thermal plasma instabilities," *Phys. Rev. Lett.*, vol. 100, p. 055001, Feb. 2008.
- [12] M. Hohenberger *et al.*, "Observation of a velocity domain cooling instability in a radiative shock," *Phys. Rev. Lett.*, vol. 105, p. 205003, Nov. 2010.
- [13] T. Clayson *et al.*, "Counter-propagating radiative shock experiments on the orion laser and the formation of radiative precursors," *High Energy Density Phys.*, vol. 23, pp. 60–72, Jun. 2017.
- [14] F. Suzuki-Vidal *et al.*, "Counterpropagating radiative shock experiments on the orion laser," *Phys. Rev. Lett.*, vol. 119, p. 055001, Aug. 2017.
- [15] J. C. Bozier, G. Thiell, J. P. Le Breton, S. Azra, M. Decroisette, and D. Schirmann, "Experimental observation of a radiative wave generated in xenon by a laser-driven supercritical shock," *Phys. Rev. Lett.*, vol. 57, no. 11, p. 1304, 1986.
- [16] S. Bouquet *et al.*, "Observation of laser driven supercritical radiative shock precursors," *Phys. Rev. Lett.*, vol. 92, no. 22, p. 225001, 2004.
- [17] M. Koenig *et al.*, "Radiative shocks: An opportunity to study laboratory astrophysics," *Phys. Plasmas*, vol. 13, p. 056504, May 2006.
- [18] C. Stehlé *et al.*, "Experimental study of radiative shocks at PALS facility," *Laser Part. Beams*, vol. 28, no. 2, pp. 253–261, Jun. 2010.
- [19] A. Dizièr *et al.*, "Highly radiative shock experiments driven by GEKKO XII," *Astrophys. Space Sci.*, vol. 336, no. 1, pp. 213–218, 2011.
- [20] R. P. Drake *et al.*, "Radiative effects in radiative shocks in shock tubes," *High Energy Density Phys.*, vol. 7, no. 3, pp. 130–140, 2011.
- [21] R. L. Singh *et al.*, "Experimental study of the interaction of two laser-driven radiative shocks at the PALS laser," *High Energy Density Phys.*, vol. 23, pp. 20–30, Jun. 2017.
- [22] G. C. Burdiak *et al.*, "The production and evolution of multiple converging radiative shock waves in gas-filled cylindrical liner Z-pinch experiments," *High Energy Density Phys.*, vol. 9, no. 1, pp. 52–62, 2013.
- [23] G. C. Burdiak *et al.*, "Radiative precursors driven by converging blast waves in noble gases," *Phys. Plasmas*, vol. 21, p. 033302, Feb. 2014.
- [24] G. C. Burdiak *et al.*, "Cylindrical liner Z-pinch experiments for fusion research and high-energy-density physics," *J. Plasma Phys.*, vol. 81, no. 3, p. 365810301, 2015.
- [25] I. H. Mitchell *et al.*, "A high impedance mega-ampere generator for fiber Z-pinch experiments," *Rev. Sci. Instrum.*, vol. 67, no. 4, p. 1533, 1995.
- [26] *Go-Araldite*. Accessed: Sep. 14, 2017. [Online]. Available: <http://www.go-araldite.com/products/epoxy-adhesives/araldite-instant-24ml-syringe>
- [27] G. F. Swadling *et al.*, "Oblique shock structures formed during the ablation phase of aluminium wire array Z-pinches," *Phys. Plasmas*, vol. 20, p. 022705, Jan. 2013.
- [28] J. J. MacFarlane, I. E. Golovkin, and P. R. Woodruff, "HELIOS-CR—A 1-D radiation-magnetohydrodynamics code with inline atomic kinetics modeling," *J. Quant. Spectrosc. Radiat. Transf.*, vol. 99, nos. 1–3, pp. 381–397, 2006.
- [29] D. D. Ryutov, "Characterizing the plasmas of dense Z-pinches," *IEEE Trans. Plasma Sci.*, vol. 43, no. 8, pp. 2363–2384, Aug. 2015.
- [30] A. Kramida, Y. Ralchenko, J. Reader, and NIST ASD Team. (2015). NIST Atomic Spectra Database (Version 5.3). Accessed: Oct. 20, 2016. National Inst. Standards Technol., Gaithersburg, MD, USA. [Online]. Available: <http://physics.nist.gov/asd>

Authors' biographies not available at the time of publication.